International Journal of Geo-Information

MDPI

Article

Monitoring and Cause Analysis of Land Subsidence along the Yangtze River Utilizing Time-Series InSAR

Yuanyuan Chen [1,*], Lin Guo [2], Jia Xu [3], Qiang Yang [1], Hao Wang [1] and Chenwei Zhu [1]

[1] College of Civil Engineering, Nanjing Forestry University, Nanjing 210037, China
[2] Key Laboratory of Mechanism, Prevention and Mitigation of Land Subsidence, Ministry of Education, Capital Normal University, Beijing 100048, China; 6382@cnu.edu.cn
[3] School of Earth Sciences and Engineering, Hohai University, Nanjing 210098, China
* Correspondence: cheny@njfu.edu.cn

Abstract: Time-series monitoring of the land subsidence in the Yangtze River coastal area is crucial for maintaining river stability and early warning of disasters. This study employed PS-InSAR and SBAS-InSAR techniques to monitor the land subsidence along the Yangtze River in Nanjing, using a total of 42 Sentinel-1A images obtained between April 2015 and November 2021. The accuracy of both methods was compared and validated, while a comprehensive analysis was conducted to ascertain the spatial distribution characteristics and underlying causes of land subsidence. The maximum deviation between the two methods and six leveling point data did not exceed ±5 mm. Within the 5 km buffer zone on either side of the Yangtze River in Nanjing, four subsidence funnels were identified. Analysis of the factors contributing to land subsidence in this area indicates that underground engineering construction and operation, increasing ground building area, and geological condition all have certain correlations to the land subsidence. The results obtained through PS-InSAR and SBAS-InSAR technologies revealed a high degree of consistency in monitoring outcomes, and the latter method exhibited superior monitoring accuracy than the former one in this area. This study holds significant implications for guiding the scientific management of urban geohazards along the Yangtze River.

Keywords: land subsidence; PS-InSAR; SBAS-InSAR; time-series analysis; area along the Yangtze River

check for updates

Citation: Chen, Y.; Guo, L.; Xu, J.; Yang, Q.; Wang, H.; Zhu, C. Monitoring and Cause Analysis of Land Subsidence along the Yangtze River Utilizing Time-Series InSAR. *ISPRS Int. J. Geo-Inf.* **2024**, *13*, 230. https://doi.org/10.3390/ijgi13070230

Academic Editor: Wolfgang Kainz

Received: 30 March 2024
Revised: 10 June 2024
Accepted: 27 June 2024
Published: 1 July 2024

Copyright: © 2024 by the authors. Licensee MDPI, Basel, Switzerland. This article is an open access article distributed under the terms and conditions of the Creative Commons Attribution (CC BY) license (https://creativecommons.org/licenses/by/4.0/).

1. Introduction

The mainstream of the Yangtze River flows through the entire territory of Jiangsu, China. The geological conditions in the Nanjing area along the river are characterized by loose geology, poor bearing capacity, and shallow groundwater levels. Due to long-term river water accumulation, the area is prone to collapse and sedimentation, resulting in land subsidence. Additionally, with the rapid development of the economy in the Yangtze River Delta region, the demand for engineering construction is increasingly expanding. Various engineering activities, such as groundwater extraction, subway engineering, and large ground building construction, have accelerated the occurrence of regional ground subsidence [1,2]. Under the joint action of the above natural and human factors, the geological environment system along the Yangtze River Delta region has been damaged, leading to urban land subsidence disasters, which, in turn, cause serious hazards such as soil collapse, road facility damage, and building wall cracking, posing a certain threat to the security of residents. Therefore, it is crucial to strengthen the monitoring and analysis of surface deformation within a certain range along the Yangtze River using advanced techniques.

Traditional approaches for ground subsidence monitoring mainly include precision leveling, trigonometric leveling, and GNSS measurements [3]. Precision leveling requires less cost, a simple construction process, and can ensure measurement accuracy. However, it is limited in the number and scope of leveling points and has a long monitoring cycle, resulting in low temporal and spatial resolution [4]. Trigonometric leveling, as an indirect

height measurement method, features minimal terrain limitations and fast measurement speed, but its accuracy is easily affected by atmospheric refraction and is difficult to calibrate [5,6]. While GNSS boasts all-weather operation, is fully automatic, and has high accuracy, the high monitoring cost makes it challenging to conduct large-scale ground subsidence monitoring [7,8]. Traditional manual measurement methods face various limitations such as measurement range, manpower consumption, timeliness, and cost. Synthetic aperture radar interferometry (InSAR), as a form of active microwave remote sensing technology enabling continuous, all-weather monitoring, can provide low-cost solutions for acquiring wide-ranging and high-precision deformation information [9–11]. Therefore, it serves as an important tool for large-scale ground deformation monitoring.

Conventional InSAR technology obtains DEM by calculating the phase difference between two SAR images [12], while D-InSAR technology utilizes DEM data for interferometric processing and filters out other phase information from the interferometric image, retaining only the deformation phase resulting from displacement [13,14]. This enables the extraction of precise ground deformation information at millimeter-level accuracy. However, the monitoring accuracy of D-InSAR is significantly hindered by various factors, including temporal and spatial decorrelation, atmospheric effects, and satellite orbit errors. Further, this method cannot monitor the development process of deformation [15,16]. To overcome the limitations and shortcomings of conventional InSAR techniques, researchers have proposed the Persistent Scatterer InSAR (PS-InSAR) [17,18] and Small Baseline Subsets InSAR (SBAS-InSAR) [19,20] approaches. These multi-temporal InSAR techniques effectively mitigate the impact of atmospheric effects and spatio-temporal decorrelation on the accuracy of surface deformation monitoring. Consequently, they have found widespread applications in various fields such as land subsidence monitoring, geological hazard assessment, and building deformation analysis [21–24].

This research acquired 42 Sentinel-1A images along the Yangtze River in Nanjing and applied PS-InSAR and SBAS-InSAR technologies to monitor and analyze the land subsidence in the area. The accuracy and reliability of the two technologies in land subsidence monitoring were evaluated through cross-validation of the continuous deformation field obtained from both techniques and comparison with external leveling data. Additionally, the causes of land subsidence in this area were analyzed from three perspectives: underground transportation engineering, building loads, and geological structure.

2. Research Area and Experimental Data

2.1. Research Area

Nanjing, situated in the lower reaches of the Yangtze River, serves as the capital of Jiangsu Province and holds strategic importance as a major intersection of the Belt and Road Initiative and the Yangtze River Economic Belt. The city is traversed by the Yangtze River, flowing from southwest to east, with its urban area encompassing significant water bodies such as the Qinhuai River, Qinhuai New River, and Xuanwu Lake. The region along both banks of the Yangtze River in Nanjing is profoundly influenced by the impact and sedimentation of river water, resulting in the formation of a broad floodplain. The geological structure in this area is characterized by soft soil, rendering it susceptible to collapse and sedimentation, and the bearing capacity is poor.

In terms of tectonic units, Nanjing is in the northern margin of the Yangtze ancient land, and the basement is mainly light metamorphic schist and metamorphic volcanic rocks. For the area along the Yangtze River in Nanjing, the overall geological conditions are not very ideal, the main characteristics are loose geology, poor bearing capacity, and shallowly buried groundwater levels. In recent years, Nanjing has experienced rapid urbanization, marked by the extensive construction of underground railways, intensive implementation of ground construction projects, and excessive exploitation of groundwater. Consequently, some areas along the Yangtze River in Nanjing have witnessed land subsidence, posing significant challenges not only to the economic development of the Yangtze River region, but also to the safety and well-being of urban residents. In light of these circumstances, this

research focused on the land subsidence along the Yangtze River, especially the 5 km buffer zone on both sides of the Yangtze River in Nanjing as a typical area for land subsidence monitoring and analysis, as shown in Figure 1. A–F were the positions of six leveling points. The findings aim to provide valuable technical insights for urban management and protection.

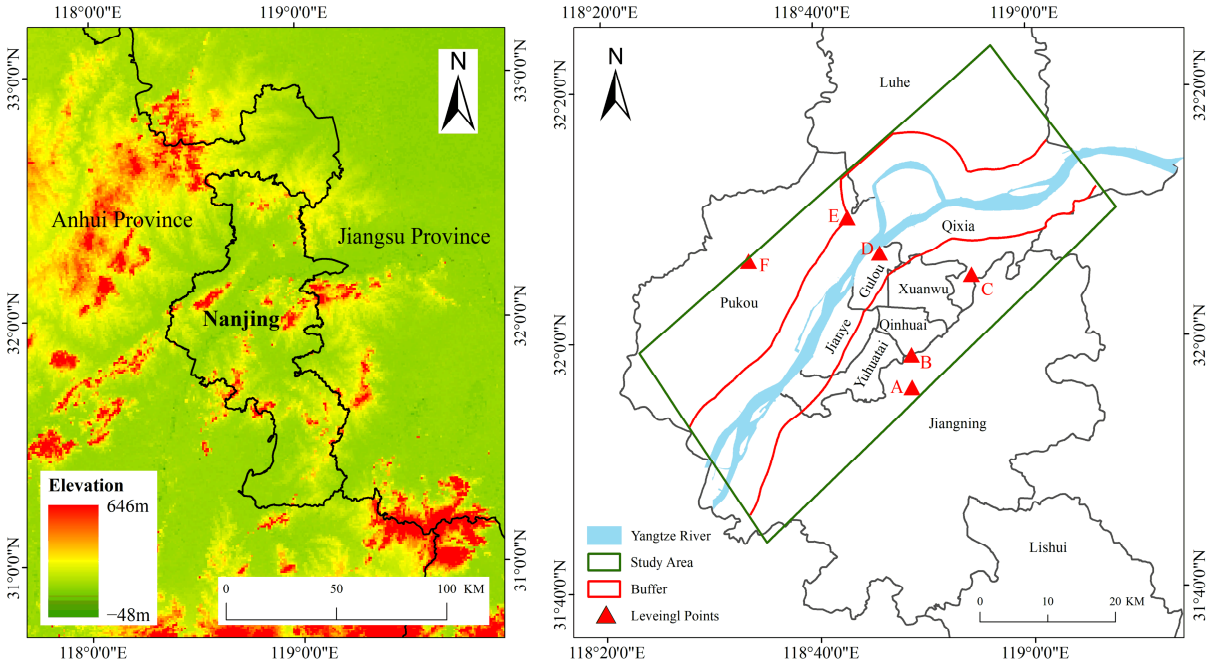


Figure 1. Study area.

2.2. Experimental Data

The Sentinel-1A satellite, operating in a solar synchronous orbit, was launched in April 2014. It is the inaugural environmental monitoring satellite deployed under the European Space Agency's Copernicus program and is equipped with a C-band SAR. Notably, it boasts high revisit frequency, wide coverage, and multiple polarimetric and working modes, which can meet the needs of time-series InSAR processing and analysis. For this study, approximately one image was selected every two months, culminating in a total of 42 Sentinel-1A images in Level-1 SLC format, which covered the areas along the Yangtze River in Nanjing from 8 April 2015 to 14 November 2021. The images were acquired in IW mode, with VV polarization, an incidence angle of 35.9°, and a spatial resolution of 5 m × 20 m (azimuthal direction × range direction). The Frame of the used data were 99 and 100, and the Path was 69.

Furthermore, this experiment utilized precision orbit data of the Sentinel-1A satellite, which was provided by the European Space Agency, to refine the orbit information. The reference digital elevation model (DEM) data utilized in this study were sourced from the SRTM elevation data with a resolution of 30 m. To validate the accuracy of the land subsidence information extracted by two methods, on-site leveling data spanning from 2015 to 2020 were employed. Figure 1 illustrates the spatial distribution of the six leveling points within the study area.

3. Technical Principles

3.1. PS-InSAR Technology

The Persistent Scatterer InSAR (PS-InSAR) technology, initially introduced by Ferretti in 2000, is designed to analyze objects within the study area that exhibit stable scattering characteristics over prolonged periods [17,18]. This involves identifying a set of ground target points with high coherence and stable reflection characteristics in image data, termed PS points, to extract phase changes. By doing this, this approach effectively avoids the problems of temporal and spatial decorrelation and reduces the influence of atmospheric effects on deformation information. As a result, PS-InSAR enables the acquisition of high-precision ground deformation information [25].

The fundamental principle of PS-InSAR technology is to select one SAR image as the master image, followed by the registration of N additional SAR images with the master image to generate N interference pairs. Subsequently, the differential processing of these pairs yields N interferograms, from which PS points with high coherence and stable reflection characteristics are extracted. Furthermore, the interference factors in phase information extraction are eliminated using orbital parameters, external DEM, and an established model. Ultimately, high-precision ground deformation information can be obtained. The interference phase of the PS point can be expressed as:

$$\varphi_{int} = \varphi_{def} + \varphi_{top} + \varphi_{fla} + \varphi_{noi} + \varphi_{atm} \quad (1)$$

Here, φ_{int} is the interference phase, φ_{def} is the deformation phase caused by the displacement of the target object during the satellite revisit cycle; φ_{fla} refers to the flat phase caused by interference on a flat surface caused by radar oblique range imaging, which can be eliminated with the assistance of precise orbital parameters; φ_{top} is the terrain phase caused by surface undulation, which can be eliminated with the assistance of DEM; φ_{atm} is the atmospheric delay phase caused by the influence of the ionosphere and troposphere on radar signals, resulting in signal propagation delay; and φ_{noi} is the phase error caused by radar thermal noise and inherent interference noise, which can be reduced by filtering.

With the assistance of precise orbit parameters and an external DEM, the interference image is flattened, and the terrain phase is eliminated. To express the relationship between the terrain residual increment and the interference phase of PS points, a model is established. Iterative calculations are performed using a linear model to estimate the surface deformation rate and the residual increment of terrain errors. Subsequently, after removing the residual deformation phase and terrain phase, further iterations are conducted to estimate the atmospheric delay phase error and noise error. This iterative process leads to the ultimate retrieval of the deformation rate and the residual elevation.

In this experiment, the selection of the master image was based on the principle of maximizing correlation among interference pairs. Ultimately, the SAR image obtained on 2 September 2019 was chosen as the master image. It was combined with the remaining 41 SAR images to form 41 interference pairs. As depicted in Figure 2, the spatial baseline exhibited a distribution primarily ranging −150~150 m, with the longest spatial baseline measuring 132.44 m and the shortest at −8.68 m. Subsequently, external DEM data were utilized to facilitate image registration and mitigate the impact of flat ground effects. The amplitude discrete index was employed to preliminarily select high-coherence target points. To obtain the initial deformation rate and residual elevation of the PS points, a linear inversion model was applied. Furthermore, high-pass filtering in space and low-pass filtering in time were employed to estimate the atmospheric delay phase. Geocoding of the PS points was accomplished using the reference DEM, with a coherence coefficient threshold of 0.7. After removing PS points with low coherence, a total of 976,871 effective PS points were obtained, enabling subsequent temporal and spatial analysis.

Due to the large coverage area of the acquired Sentinel-1A image, the processing was time-consuming. As a result, 42 images were cropped using geocoded vector data, and subsequent experimental processing was carried out based on these cropped images.

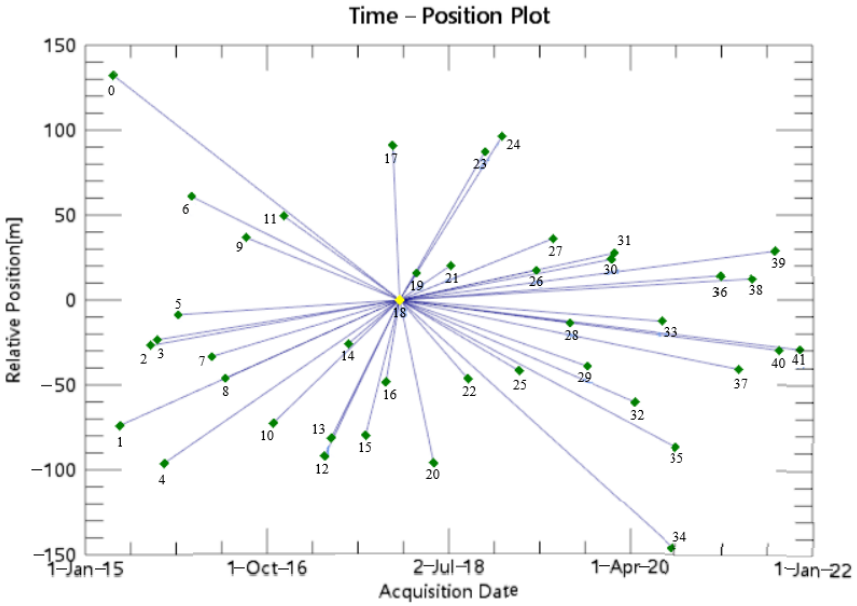


Figure 2. Image pairs and baselines generated by PS-InSAR.

3.2. SBAS-InSAR Technology

The Small Baseline Subset InSAR (SBAS-InSAR) technique was initially proposed by Berardino et al. in 2002 [19]. The fundamental concept of SBAS-InSAR technology involves the selection of M SAR images for flexible combination, ensuring that each image forms at least one interference pair with another image. By establishing thresholds for temporal and spatial baselines to exclude image data that do not meet the criteria, the adverse effects of spatiotemporal incoherence on monitoring results are mitigated. Subsequently, following the small baseline combination principle, differential interference processing is performed on all image pairs to derive N differential interferograms. The flat-earth phase and terrain phase in the interference phase are eliminated by removing the flat-earth effect and leveraging external DEM data. The interferometric phase of the interferogram generated by two SAR images can be expressed as the following formula,

$$\varphi = \varphi_1 - \varphi_2 = \frac{4\pi}{\lambda} \cdot (d_1 - d_2) + \Delta\varphi_{toperror} + \varphi_{atm} + \varphi_{noi} \quad (2)$$

Here, φ_1 and φ_2 are the interferometric phases obtained at the imaging time of two SAR images, respectively. $\Delta\varphi_{toperror}$ is the residual terrain phase error, and φ_{atm} is the atmospheric delay phase. φ_{noi} is the noise phase. In general, SBAS-InSAR technology operates under the assumption that surface deformation follows a linear pattern, and hence, a linear model was constructed to characterize the surface deformation. The residual terrain phase present in the interferometric phase was estimated and removed using the singular value decomposition method. Additionally, the atmospheric phase and nonlinear deformation phase were eliminated through spatial domain low-pass filtering and time domain high-pass filtering. Subsequently, the least-squares method was employed to calculate the average phase change rate and surface deformation for each given time.

In this experiment, the spatial baseline threshold was set to 48%, and the time baseline threshold was 180 days. The SAR image acquired on 7 September 2018 was selected as the master image. The generated image pairs and baselines are illustrated in Figure 3. Subsequently, the interference processing was assisted by external DEM data. The Goldstein filtering method and the Delaunay MCF unwrapping method were employed [26]. After evaluating the noise area in the unwrapping output and considering the phase information of the research area, the coherence threshold was finally set at 0.2. Following this, orbit refinement and re-phasing were conducted. The residual terrain error and atmospheric delay phase were estimated using two inversions, and finally, geocoding was performed.

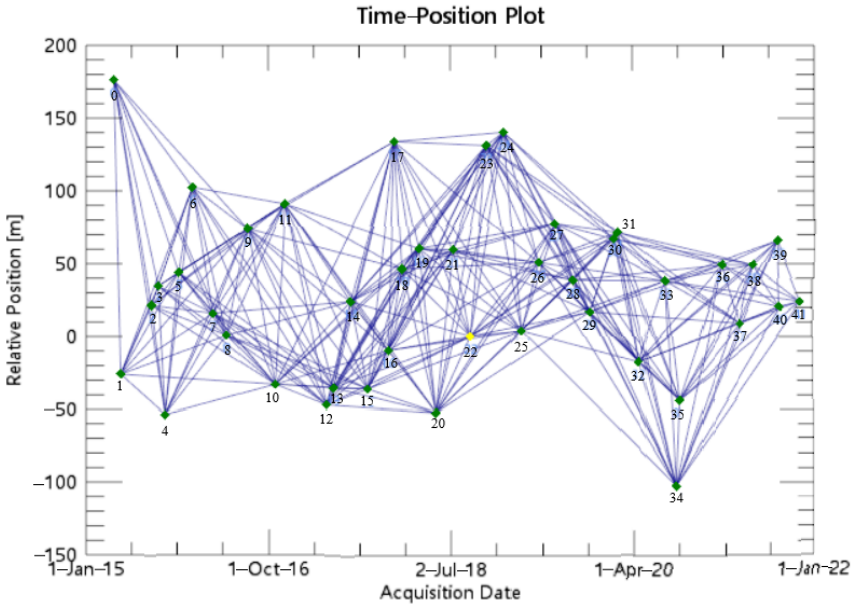


Figure 3. Image pairs and baselines generated by SBAS-InSAR.

4. Results Analysis

4.1. Comparative Validation of PS-InSAR and SBAS-InSAR Monitoring Results

In this study, PS-InSAR and SBAS-InSAR were employed to monitor the land subsidence using 42 Sentinel-1A SAR images. Figures 4 and 5 depict the distribution of Line-of-Sight (LOS) subsidence rates obtained from the two time-series InSAR methods, providing a clear and intuitive visualization of the land subsidence in the study area. The range of land LOS subsidence rates observed by PS-InSAR fell between −19.9 mm/a and 22.0 mm/a, while those derived from SBAS-InSAR were found to range from −12.1 mm/a to 17.7 mm/a.

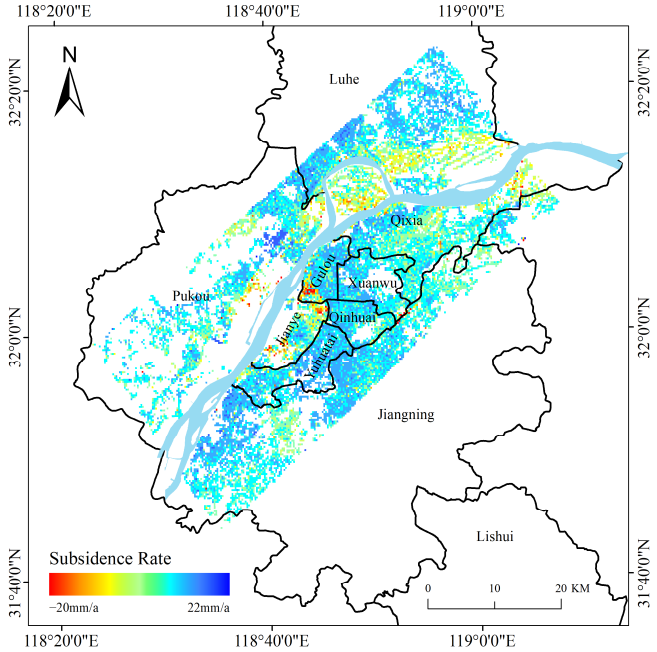


Figure 4. PS-InSAR monitoring results based on Sentinel-1A images.

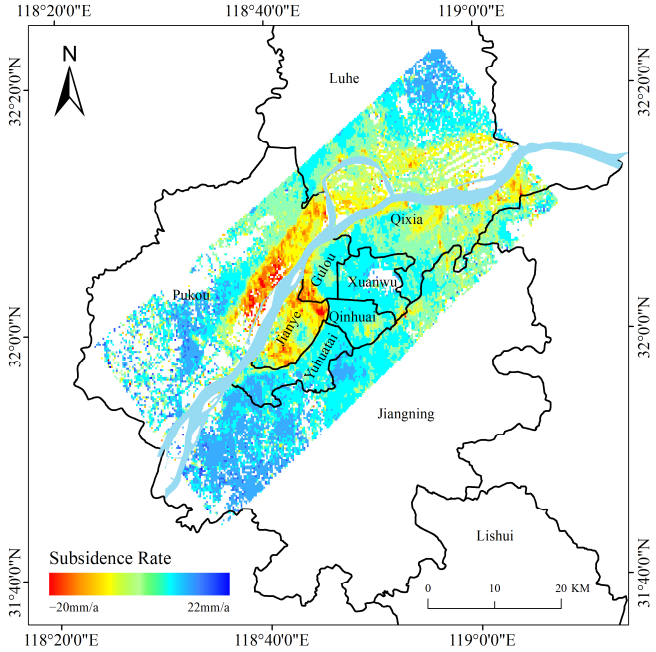


Figure 5. SBAS-InSAR monitoring results based on Sentinel-1A images.

To validate the reliability of the experimental findings in this paper, the results obtained from the two time-series analysis methods were subjected to linear fitting analysis. Linear fitting is a statistical modeling approach used to establish a linear relationship between variables [27]. The least-squares method is usually utilized to determine the most suitable fitting line [28]. The correlation coefficient, which assesses the degree of linear correlation between the two variables, was employed. The coefficient of determination R^2, ranging between 0 and 1, was utilized to gauge the goodness of fit of the model. In cases where variables exhibit linear correlation, the coefficient of determination represents the square of the correlation coefficient. The subsidence points sharing identical latitude and longitude were extracted from the outcomes of both PS-InSAR and SBAS-InSAR, facilitating a comparison of the linear relationship between the subsidence of these points observed by the two methods. As illustrated in Figure 6, the annual average land subsidence rates of 2462 subsidence points with the same latitude and longitude underwent linear fitting and analysis. It is evident that the points, with the PS-InSAR monitoring results plotted as vertical coordinates and the SBAS-InSAR monitoring results as horizontal coordinates, exhibit uniform distribution on either side of the fitting line. The coefficient of determination R^2 is 0.76, which indicates a high degree of consistency between the two processing outcomes.

4.2. Accuracy Verification of Monitoring Results Based on Leveling Data

This experiment utilized the leveling data from the region to validate the accuracy of these two methods. A total of six leveling points was chosen as reference points for testing the two time-series InSAR monitoring results. The locations of these reference leveling points are displayed in Figure 1. In order to ensure the correctness of the comparative analysis, the results of PS-InSAR and SBAS-InSAR were converted from LOS direction to vertical direction.

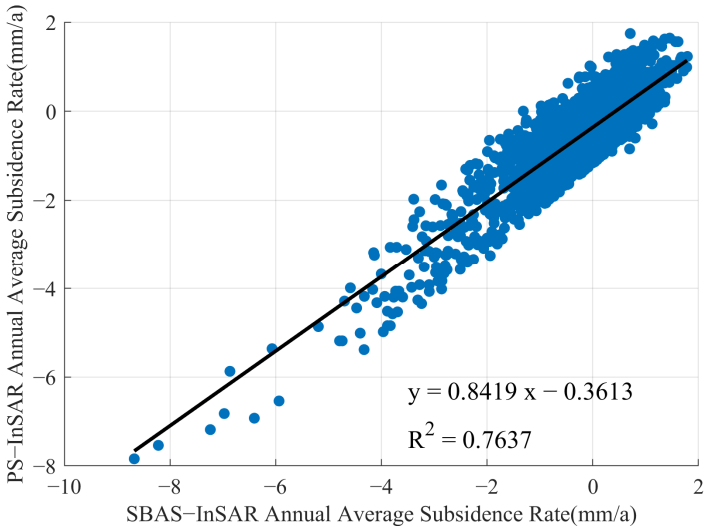


Figure 6. Comparison and validation of monitoring results between PS-InSAR and SBAS-InSAR.

To facilitate year-to-year comparisons, subsidence points with similar latitude and longitude to the same reference leveling points were extracted. Subsidence results from 2015 (from April to December) and 2016–2020 (from January to December) were selected for comparison with the leveling data in the corresponding time range. The errors between the leveling data and the deformation obtained by the two time-series InSAR techniques are shown in Figures 7 and 8. Figure 7 shows the comparison of deformation results of six points in three monitoring data at different times. Figure 8 shows the comparison of the deformation of each point obtained from the three monitoring data between 2015 and 2021. The maximum error between the PS-InSAR monitoring results and the leveling data was 4.54 mm, the minimum error was 0.02 mm, and the root mean square error was 2.12 mm. Meanwhile, the maximum error, minimum error, and root mean square between the SBAS-InSAR monitoring results and the leveling data were 4.15 mm, 0.14 mm, and 1.60 mm, respectively. These results suggest that both PS-InSAR and SBAS-InSAR are highly accurate methods for extracting ground deformation, as evidenced by the very small deviations between the monitoring results of the two methods and the leveling data. Notably, the maximum deviation did not exceed ±5 mm.

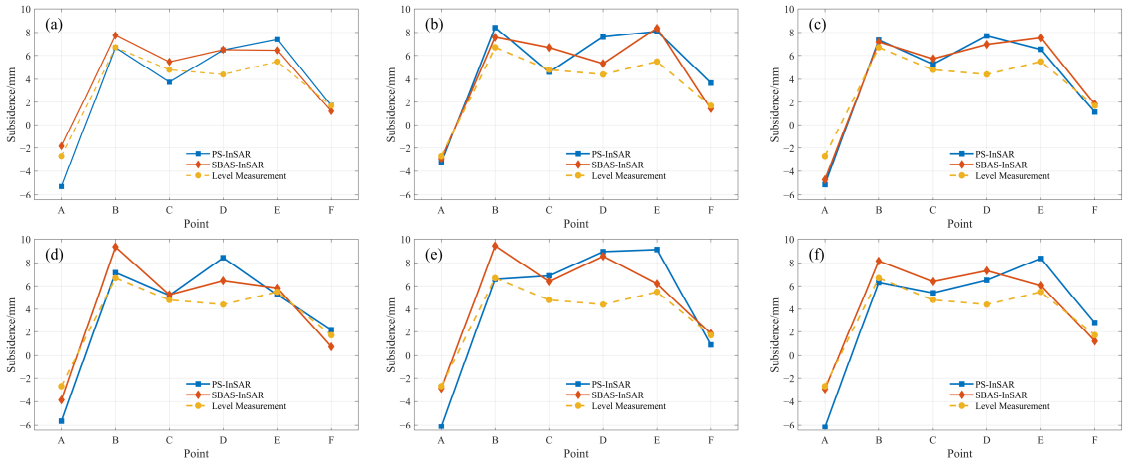


Figure 7. Accuracy comparisons between annual monitoring results from PS-InSAR and SBAS-InSAR and leveling data. (**a**) 2015.04–2015.12, (**b**) 2016.01–2016.12, (**c**) 2017.01–2017.12, (**d**) 2018.01–2018.12, (**e**) 2019.01–2019.12, (**f**) 2020.01–2020.12.

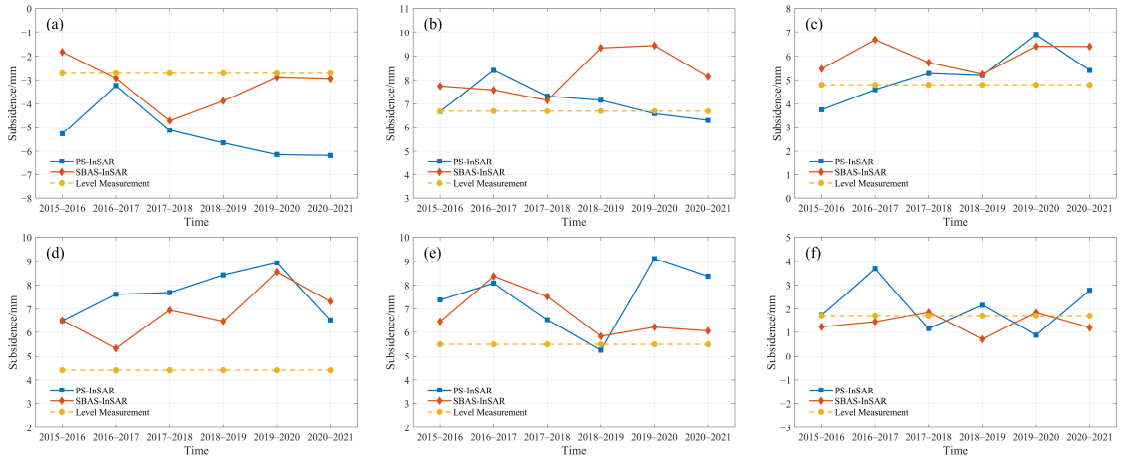


Figure 8. Accuracy comparison of PS-InSAR and SBAS-InSAR monitoring results with leveling data at each point from 2015 to 2021. (**a**) Point A, (**b**) point B, (**c**) point C, (**d**) point D, (**e**) point E, (**f**) point F.

To further illustrate the high correlation between the PS-InSAR and SBAS-InSAR monitoring results and the leveling data, the two monitoring results were subjected to linear fitting with the leveling data, and the fitting results are presented in Figure 9. The fitting results reveal an even distribution of points, with SBAS-InSAR and PS-InSAR monitoring results as the horizontal coordinates and leveling results as the vertical coordinates, on both sides of the fitting line. The coefficient of determination R2 between the PS-InSAR results and the leveling data was 0.8893, and that between the SBAS-InSAR results and the leveling data was 0.9381, indicating a high degree of correlation between the monitoring results of the two methods and the leveling data. These findings emphasize the reliability of land subsidence monitoring results based on PS-InSAR and SBAS-InSAR. Notably, in areas along the Yangtze River, especially where numerous high-rise buildings create strong dihedral scattering, the determination coefficient of SBAS-InSAR and leveling data exceeded that of PS-InSAR and leveling data, suggesting that SBAS-InSAR is more suitable for monitoring land subsidence in this area.

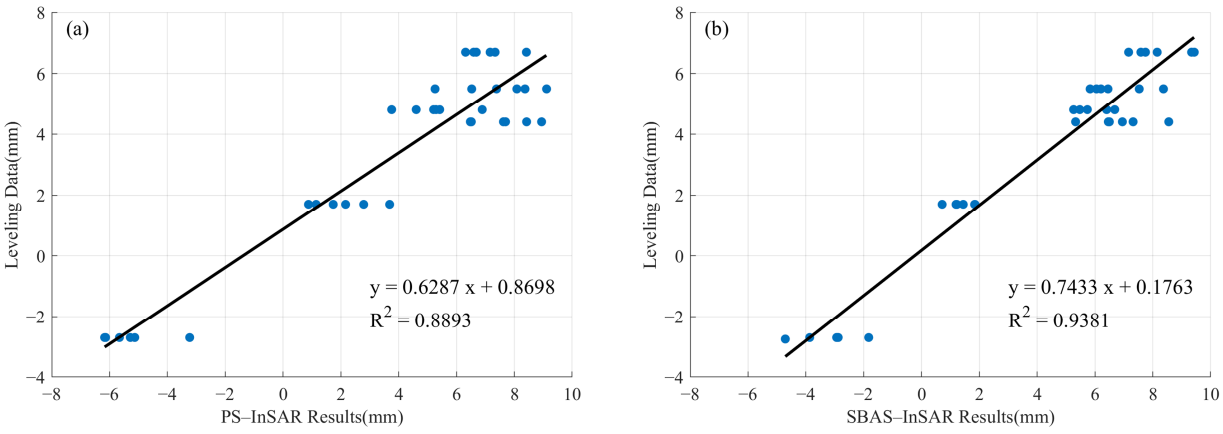


Figure 9. Linear fitting between leveling data and InSAR monitoring results. (**a**) PS-InSAR fitting results; (**b**) SBAS-InSAR fitting results.

4.3. Analysis of Spatiotemporal Variation Characteristics of Land Subsidence

A 5 km buffer zone was established on both sides of the Yangtze River, and the SBAS-InSAR results were cropped to obtain the average annual subsidence rate along the river. The spatial and temporal variation characteristics of land subsidence were analyzed in this buffer zone as the key area. Figure 10 displays the LOS subsidence and uplift areas, represented by red and blue colors, respectively. The ground deformation in the 5 km buffer

showed stability from April 2015 to November 2021, with the annual average subsidence rate ranging from −12.5 mm/a to 17.2 mm/a. Within the buffer zone, there were four main subsidence areas, which were located at the area of the northeast of Jianye District and the southwest of Gulou District (S1), the eastern riverside area of Pukou District (S2), the Baguazhou area (S3), and the Longtan Street in the eastern part of Qixia District (S4). From 2015 to 2021, the spatial distribution of land subsidence in the buffer zone was relatively concentrated. Most areas in the northeast showed a slow sinking trend, with an average annual deformation rate ranging from −10 mm/a to 0 mm/a, while some areas in the southwest showed an upward trend, with an average annual deformation rate ranging from 0 mm/a to 10 mm/a.

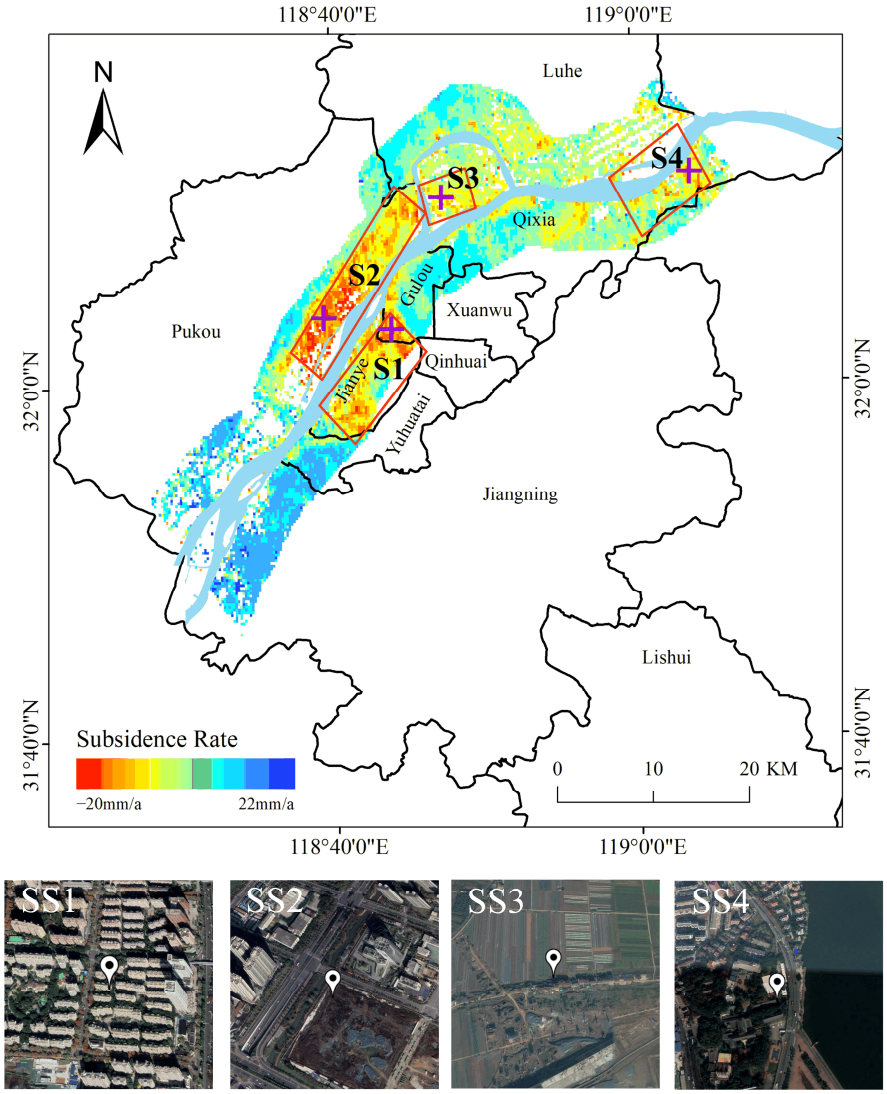


Figure 10. SBAS-InSAR monitoring results of the 5 km buffer zone along the Yangtze River from 2015 to 2021.

The distribution of the main subsidence areas in Figure 10 reveals a distinct pattern. It can be seen that the subsidence funnel S1 was gradually converging into a larger area. Notably, the southwest area of S1 near the Yuzui Wetland Park in Jianye District exhibited a maximum LOS subsidence rate of −10.4 mm/a, attributed to complex geological conditions. This area comprised an upper soil layer of alternating marshes and shoals of silty clay, and the lower part was the riverbed facies layer composed of medium to fine sand, making it susceptible to subsidence. The northeast area of S1, situated at the junction of the northeast of Jianye District and the southwest of Gulou District (now the Hexi development new

area), experienced a maximum LOS deformation rate of −13.6 mm/a. In recent years, the area has been surrounded by high-rise buildings and developed rapidly. Metro Line 2 and Metro Line 10 passed through this area. Therefore, large-scale ground and underground construction was one of the main reasons for the formation of a subsidence funnel in this area. S2 was a super-large subsidence area composed of Jiangpu Street, Dingshan Street, Mount Taishan Street, and Yanjiang Street in Pukou District. This area boasted three metro lines and seven subway stations, with a maximum LOS subsidence rate of −13.5 mm/a. The subsidence rate of this region was directly influenced by its development planning. In June 2015, the Jiangbei New Area of Nanjing was established, formally commencing construction in 2017. The period from 2017 to 2022 witnessed rapid five-year growth in Nanjing Jiangbei New Area. The significant subsidence in this area primarily resulted from high-intensity underground engineering operations and alterations in surface loading. Area S3 was located in the southern part of Baguazhou, Qixia District, exhibiting a maximum LOS subsidence rate of −8.8 mm/a. Baguazhou, a large island in the Yangtze River, is marked by the division of the Yangtze River into its northern and southern branches. Despite the low building density and predominance of farmland, which minimizes the impact of human factors, the area's geological conditions are not stable due to its formation as a sandbar-type plain in the middle of the Yangtze River through alluvial action. Area S4, situated near Longtan Street along the river in the eastern part of Qixia District, exhibited a maximum LOS subsidence rate of −9.2 mm/a. This area falls within the Ningzhen folded belt and is characterized by soft soil. Given the presence of wharf companies, as well as multiple logistics and warehousing firms in the area, it is prone to subsidence.

To analyze the temporal characteristics of land subsidence in key areas along the Yangtze River in Nanjing, we selected four points with the highest LOS subsidence rates within the four identified subsidence funnels as representative feature points. Using these feature points, we generated a cumulative subsidence change map spanning the entire period. The spatial distribution of the four selected subsidence points is illustrated in Figure 10, while the SBAS-InSAR deformation curves for these four points are displayed in Figure 11. It is evident that between April 2015 and November 2021, all these four points exhibited distinct and varying patterns of uneven subsidence.

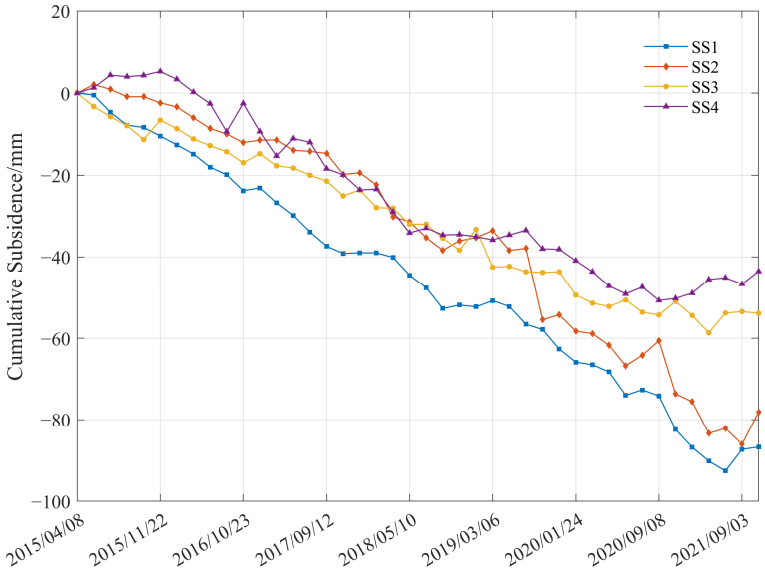


Figure 11. The time-series deformation trend of the feature points in the main subsidence area of SBAS-InSAR from 2015 to 2021.

As depicted in Figures 10 and 11, the feature point SS1 was located close to Jiangdong Street, Mochou Lake Street, and Binhu Street, with Metro Line 2 passing through. The LOS cumulative subsidence at SS1 amounted to −86.7 mm. This subsidence can be attributed to the excessive building density and load in this area, as analyzed earlier. The SS2 point, situated near Jiangpu Street in Pukou District, exhibited an overall gradual subsidence trend, with an LOS cumulative total subsidence of −78.1 mm. However, there were two rapid subsidence trends in 2019 and 2021, which can be closely linked to the development plan of the area. Point SS3 was situated in the Baguazhou area. While there was a slight rebound observed on the ground over a relatively short period, the overall trend of subsidence remained slow and stable. The LOS cumulative total subsidence at SS3 amounted to −53.8 mm. This trend can be attributed to the unstable geological conditions prevalent in the area. The LOS cumulative settlement at point SS4, situated in Longtan Street, Qixia District, has reached −43.5 mm, indicating a generally stable sinking trend, but with a noted rebound since September 2020.

5. Discussion of the Factors Related to Land Subsidence along the Yangtze River in Nanjing

5.1. The Influence of Underground Engineering on Land Subsidence

The construction of subway tracks is one of the key directions for the future development of cities. However, this infrastructure also impacts the soil structure, leading to urban land subsidence issues [29]. In this study, we aimed to investigate the influence of subway operation on urban land subsidence by analyzing the SBAS-InSAR subsidence monitoring results of three stations (Wanhuicheng Stantion, Linjing Station, and Lvboyuan Station) on Nanjing Metro Line 10 after they started operating in 2014. Figure 12 represents the subsidence distribution near the three subway stations during 2015 and 2021.

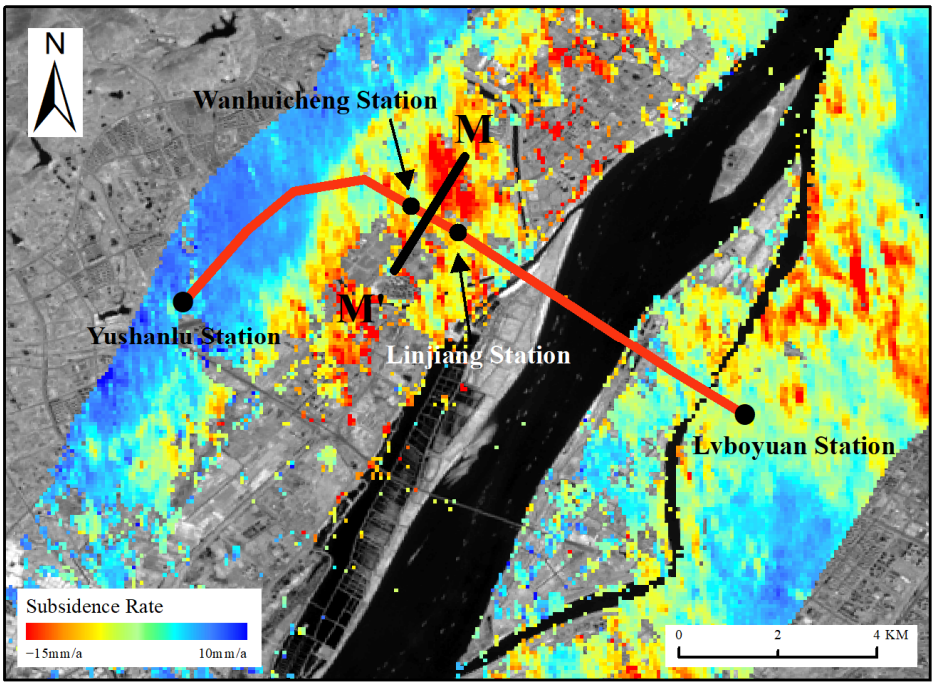


Figure 12. SBAS-InSAR LOS subsidence rate of some subway stations on Nanjing Metro Line 10.

As illustrated in Figure 12, the area has been undergoing low-speed subsidence since the three stations started operating in 2014. The primary subsidence-prone areas were concentrated near Wanhuicheng Station and Linjiang Station, both located in Pukou. Notably, the area between these two stations had been experiencing the most severe subsidence, and the area near Lvboyuan Station also exhibit a certain degree of subsidence, but it was smaller than that near Wanhuicheng and Linjiang Station.

To analyze the characteristics of the transverse ground deformation changes near Wanhuicheng and Lingjiang Stations, a transverse profile line MM′ across the subway line was selected in an area with serious subsidence. Subsidence rates of the points on the profile line were extracted for further analysis. Figure 13 shows the spatial distribution of subsidence rates on the transverse section line. The results indicated that the subsidence rates of the points on the MM′ profile line were unevenly distributed on both sides of the subway, with many small fluctuations. The LOS subsidence rates on the M side were significantly faster than that on the M′ side, and the LOS subsidence rates were in the range from −13.32 mm/a to −2.67 mm/a, which showed a general sinking trend. The different degrees of land subsidence around these subway stations indicate that there may be a certain relationship between subway station operation and ground subsidence. To prevent the occurrence of various situations, such as structural damage and safety hazards, regular monitoring and maintenance are necessary.

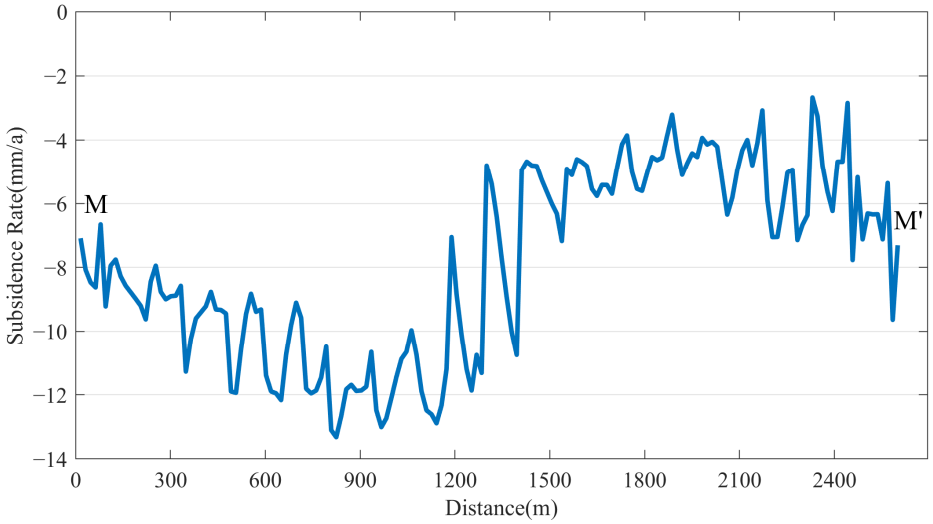


Figure 13. The LOS subsidence rates of the points on the MM′ profile line.

5.2. The Relationship between Ground Building Area and Land Subsidence

The acceleration of urbanization has increased a load of construction projects on the urban ground, which, in turn, poses a risk of land subsidence [30,31]. To investigate the impact of urban construction on land subsidence along the Yangtze River in Nanjing, the Landsat8 OLI images from 2016, 2019, and 2021 were used in this experiment to extract the ground buildings in the subsidence funnel areas. Based on the normalized building index (NDBI) obtained from Landsat 8, the ground buildings were extracted, and the areas were calculated [32]. The results found that the areas of ground building in the subsidence funnels along the Yangtze River have steadily increased from 2015 to 2021, as shown in Figure 14. By comparing the time-series deformation trend of the key feature points (Figure 11) extracted by SBAS-InSAR technology with the ground building areas, the impact of the building area changing on land subsidence was analyzed. Figure 14 shows that as the ground building areas continued to increase during 2016–2021, the cumulative subsidence of the feature points in the areas also increased. It can be inferred that the increase of ground building area brought by urban expansion is positively correlated with land subsidence to some extent.

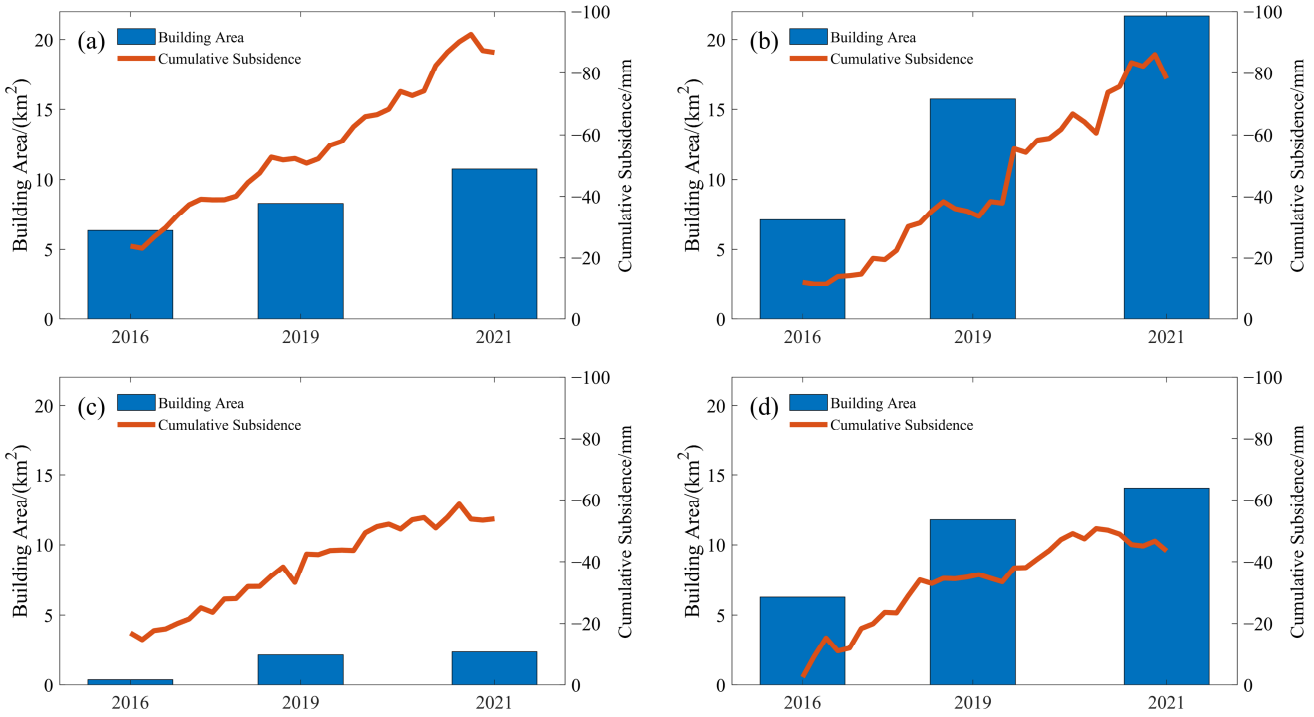


Figure 14. Relationship between LOS cumulative subsidence of the feature points and ground building area in subsidence funnels. (**a**) Area S1, (**b**) area S2, (**c**) area S3, (**d**) area S4.

5.3. The Influence of Geological Structure on Land Subsidence

The floodplain on both sides of the Yangtze River in Nanjing is broad. According to its topographic features, geomorphological units, and geotechnical combination, it can be classified as a floodplain soft soil area. This area primarily consists of Quaternary sedimentary soft soil layers that have been formed through the deposition and siltation process of the Yangtze River [33]. As a result, its geological composition is loose, resulting in poor bearing capacity. The structural characteristics of the soft soil layers in the Yangtze River floodplain are summarized in Table 1.

Table 1. Structural characteristics of the soft soil layer in the Yangtze floodplain.

Soil Layer	Characteristic
Surface recent and outdated fill	Mainly composed of building residue and cultivated soil, which is soft and has strong plasticity
Marsh facies with mucky and silty clay	Pure without sand, showing grayish-brown
Floodplain facies with muddy, silty clay and silt sand interbedding	With horizontal bedding and grey colors
Riverbed facies with medium-coarse gravel sand, coarse gravel sand mixed with gravel or boulders	Compactness increases with depth from loose to dense

According to Table 1, it can be seen that the floodplain of Nanjing along the Yangtze River predominantly consists of clay soil with high dispersion, strong hydrophilicity, a large void ratio, and high saturation. Owing to its thixotropic properties, this type of soil is susceptible to surface deformation when subjected to specific loads or high-intensity disturbances. Furthermore, excessive groundwater extraction and high-intensity engineering activities can disrupt the loose structure of the soft soil layer, rendering it more vulnerable to geological hazards such as subsidence, landslides, and soft foundations. The four primary subsidence areas identified in this study were all distributed within a 5 km

radius along the Yangtze River. This led to the inference that the geological structure of this study area constitutes a significant factor contributing to land subsidence.

6. Conclusions

In this paper, two time-series technologies, PS-InSAR and SBAS-InSAR, were used to monitor the land subsidence in Nanjing along the Yangtze River using 42 Sentinel-1A images from April 2015 to November 2021. The following conclusions can be drawn:

(1) The ground deformation along the Yangtze River in Nanjing extracted by PS-InSAR and SBAS-InSAR technologies was consistent, and the two monitoring results had a high correlation with the leveling results. The maximum deviation of deformation didn't exceed ±5 mm, which was reliable in accuracy.

(2) The key areas within 5 km on both sides of the Yangtze River were analyzed. It was found that there were four subsidence funnels from 2015 to 2011, which were distributed in Jianye District and the southwest of Gulou District, the eastern riverside area of Pukou District, the Baguazhou area, and the Longtan Street in the eastern part of Qixia District, respectively. The subsidence in Jianye District was the most severe, and there was a trend of gradually connecting into a large subsidence funnel. The maximum LOS cumulative subsidence of Jianye district was −86.7 mm. The subsidence area along the river in Dingshan Street of Pukou District was the largest subsidence funnel in the study area. The maximum LOS cumulative subsidence reached −78.1 mm.

(3) The land subsidence along the Yangtze River has a certain correlation with the increasing of the ground building area, the construction and operation of some underground engineering such as subway stations, and the geological conditions of the region, but the contribution of each factor to the subsidence needs to be further analyzed in future studies.

Author Contributions: Conceptualization, Yuanyuan Chen, Lin Guo and Jia Xu; methodology, Yuanyuan Chen and Lin Guo; software, Qiang Yang, Hao Wang and Chenwei Zhu; validation, Yuanyuan Chen, Lin Guo, Jia Xu, Qiang Yang and Hao Wang; formal analysis, Jia Xu and Lin Guo; investigation, Yuanyuan Chen, Qiang Yang and Hao Wang; resources, Yuanyuan Chen; data curation, Hao Wang and Chenwei Zhu; writing—original draft preparation, Yuanyuan Chen and Lin Guo; writing—review and editing, Jia Xu, Qiang Yang and Chenwei Zhu; visualization, Hao Wang; supervision, Yuanyuan Chen; project administration, Yuanyuan Chen; funding acquisition, Lin Guo. All authors have read and agreed to the published version of the manuscript.

Funding: This research was funded by the Jiangsu Water Conservancy Science and Technology Project, grant number 2019001, the National Natural Science Foundation of China, grant number 41930109, and the Key Laboratory of Land satellite Remote sensing Application, Ministry of Natural Resources of the People's Republic of China, grant number KLSMNR-G202311.

Data Availability Statement: The data that support the findings of this study are available from the corresponding author upon reasonable requests.

Acknowledgments: The Sentinel-1A images were freely provided by the European Space Agency.

Conflicts of Interest: The authors declare no conflicts of interest.

References

1. Na, T.; Kawamura, Y.; Kang, S.S.; Utsuki, S. Hazard mapping of ground subsidence in east area of Sapporo using frequency ratio model and GIS. *Geomat. Nat. Hazards Risk* **2021**, *12*, 347–362. [CrossRef]
2. Bagheri-Gavkosh, M.; Hosseini, S.M.; Ataie-Ashtiani, B.; Sohani, Y.; Ebrahimian, H.; Morovat, F.; Ashrafi, S. Land subsidence: A global challenge. *Sci. Total Environ.* **2021**, *778*, 146193. [CrossRef] [PubMed]
3. Ding, X.L.; Liu, G.X.; Li, Z.L.; Li, Z.; Chen, Y.Q. Ground subsidence monitoring in Hong Kong with satellite SAR interferometry. *Photogramm. Eng. Remote Sens.* **2004**, *70*, 1151–1156. [CrossRef]

4. Yalçınkaya, M. Monitoring crustal movements in west Anatolia by precision leveling. *J. Surv. Eng.* **2003**, *129*, 44–49. [CrossRef]
5. Nestorović, Ž.; Delčev, S. Comparison of height differences obtained by trigonometric and spirit leveling method. *Geonauka* **2014**, *2*, 30–37. [CrossRef]
6. Yang, D.L.; Zou, J.; Shen, Y.W.; Zhu, H. Research and application of trigonometric leveling to replace precise leveling. *J. Surv. Eng.* **2021**, *147*, 04021012.
7. Xiang, Y.F.; Wang, H.; Chen, Y.Y.; Xing, Y. GNSS imaging of strain rate changes and vertical crustal motions over the Tibetan Plateau. *Remote Sens.* **2021**, *13*, 4937. [CrossRef]
8. Xiang, Y.F.; Yue, J.P.; Liu, G.; Chen, Y.Y. Characterizing the spatial patterns of vertical crustal deformations over the South American continent based on GNSS imaging. *Pure Appl. Geophys.* **2022**, *79*, 3569–3587. [CrossRef]
9. Zhu, J.J.; Li, Z.W.; Hu, W.J. Research progress and methods of InSAR for deformation monitoring. *Acta Geod. Cartogr. Sin.* **2017**, *46*, 1717–1733.
10. Wang, Y.; Feng, G.; Li, Z.; Luo, S.; Wang, H.; Xiong, Z.; Zhu, J.; Hu, J. A strategy for variable-scale InSAR deformation monitoring in a wide area: A case study in the Turpan–Hami Basin, China. *Remote Sens.* **2022**, *14*, 3832. [CrossRef]
11. Wang, Z.; Dai, H.; Yan, Y.; Ren, J.; Zhang, Y.; Liu, J. An InSAR deformation phase retrieval method combined with reference phase in mining areas. *Remote Sens.* **2023**, *15*, 4573. [CrossRef]
12. Feng, Y.; Zhou, Y.; Chen, Y.; Li, P.; Xi, M.; Tong, X. Automatic selection of permanent scatterers-based GCPs for refinement and reflattening in InSAR DEM generation. *Int. J. Digit. Earth* **2022**, *15*, 954–974. [CrossRef]
13. Fan, H.; Deng, K.; Ju, C.; Zhu, C.; Xue, J. Land subsidence monitoring by D-InSAR technique. *Min. Sci. Technol.* **2011**, *21*, 869–872. [CrossRef]
14. Fan, H.; Wei, G.; Yong, Q.; Xue, J.; Chen, B. A model for extracting large deformation mining subsidence using D-InSAR technique and probability integral method. *Trans. Nonferrous Met. Soc.* **2014**, *24*, 1242–1247. [CrossRef]
15. Chen, Y.; Yu, S.; Tao, Q.; Liu, G.; Wang, L.; Wang, F. Accuracy verification and correction of D-InSAR and SBAS-InSAR in monitoring mining surface subsidence. *Remote Sens.* **2021**, *13*, 4365. [CrossRef]
16. Wang, L.; Deng, K.; Zheng, M. Research on ground deformation monitoring method in mining areas using the probability integral model fusion D-InSAR, sub-band InSAR and offset-tracking. *Int. J. Appl. Earth Obs.* **2020**, *85*, 101981. [CrossRef]
17. Ferretti, A.; Prati, C.; Rocca, F. Analysis of permanent scatterers in SAR interferometry. In Proceedings of the IEEE 2000 International Geoscience and Remote Sensing Symposium, Honolulu, HI, USA, 24–28 July 2000; pp. 761–763.
18. Ferretti, A.; Prati, C.; Rocca, F. Permanent scatterers in SAR interferometry. *IEEE Trans. Geosci. Remote Sens.* **2001**, *39*, 8–20. [CrossRef]
19. Berardino, P.; Fornaro, G.; Lanari, R.; Sansosti, E. A new algorithm for surface deformation monitoring based on small baseline differential SAR interferograms. *IEEE Trans. Geosci. Remote Sens.* **2002**, *40*, 2375–2383. [CrossRef]
20. Boloorani, A.D.; Darvishi, M.; Weng, Q.; Liu, X. Post-war urban damage map** using InSAR: The case of Mosul City in Iraq. *ISPRS Int. J. Geo-Inf.* **2021**, *10*, 140. [CrossRef]
21. Joshi, M.; Kothyari, G.C.; Kotlia, B.S. Landslide detection in Kinnaur Valley, NW India using PS-InSAR technique. *Phys. Geogr.* **2024**, *45*, 160–174. [CrossRef]
22. Liu, J.; Li, T.; Ma, S.; Shan, Q.; Jiang, W. Study on LOS to Vertical Deformation Conversion Model on Embankment Slopes Using Multi-Satellite SAR Interferometry. *ISPRS Int. J. Geo-Inf.* **2024**, *13*, 58. [CrossRef]
23. Welikanna, D.R.; Jin, S.Y. Investigating ground deformation due to a series of collapse earthquakes by means of the PS-InSAR technique and Sentinel 1 data in Kandy, Sri Lanka. *J. Appl. Remote Sens.* **2023**, *17*, 014507. [CrossRef]
24. Zhang, P.; Guo, Z.; Guo, S.; Guo, S.; Xia, J. Land subsidence monitoring method in regions of variable radar reflection characteristics by integrating PS-InSAR and SBAS-InSAR techniques. *Remote Sens.* **2022**, *14*, 3265. [CrossRef]
25. Malik, K.; Kumar, D.; Perissin, D.; Pradhan, B. Estimation of ground subsidence of New Delhi, India using PS-InSAR technique and Multi-sensor Radar data. *Adv. Space Res.* **2022**, *69*, 1863–1882. [CrossRef]
26. Bahti, F.N.; Chung, C.C.; Lin, C.C. Parametric Test of the Sentinel 1A Persistent scatterer-and small baseline subset-interferogram Synthetic Aperture Radar processing using the stanford method for persistent scatterers for practical landslide monitoring. *Remote Sens.* **2023**, *15*, 4662. [CrossRef]
27. Cao, Y.; Li, P.; Hao, D.; Lian, Y.; Wang, Y.; Zhao, S. Analysis of the relationship between vegetation and radar interferometric coherence. *Sustainability* **2022**, *14*, 16471. [CrossRef]
28. Krystek, M.; Anton, M. A weighted total least-squares algorithm for fitting a straight line. *Meas. Sci. Technol.* **2007**, *8*, 3438. [CrossRef]
29. Xu, Y.; Ma, L.; Du, Y.; Shen, S. Analysis of urbanisation-induced land subsidence in Shanghai. *Nat. Hazards* **2012**, *63*, 1255–1267. [CrossRef]
30. Cui, Z.; Yang, J.; Yuan, L. Land subsidence caused by the interaction of high-rise buildings in soft soil areas. *Nat. Hazards* **2015**, *79*, 1199–1217. [CrossRef]
31. Yang, Q.; Ke, Y.; Zhang, D.; Chen, B.; Gong, H.; Lv, M.; Zhu, L.; Li, X. Multi-scale analysis of the relationship between land subsidence and buildings: A case study in an eastern Beijing urban area using the PS-InSAR technique. *Remote Sens.* **2018**, *10*, 1006. [CrossRef]

32. Karanam, H.K.; Neela, V.B. Study of normalized difference built-up (NDBI) index in automatically mapping urban areas from Landsat TN imagery. *Int. J. Eng. Sci. Math.* **2017**, *8*, 239–248.
33. Saito, Y.; Yang, Z.S.; Hori, K. The Huanghe (Yellow River) and Changjiang (Yangtze River) deltas: A review on their characteristics, evolution and sediment discharge during the Holocene. *Geomorphology* **2001**, *41*, 219–231. [CrossRef]

Disclaimer/Publisher's Note: The statements, opinions and data contained in all publications are solely those of the individual author(s) and contributor(s) and not of MDPI and/or the editor(s). MDPI and/or the editor(s) disclaim responsibility for any injury to people or property resulting from any ideas, methods, instructions or products referred to in the content.